JOURNAL OF SPACECRAFT AND ROCKETS
Vol. 36, No. 2, March–April 1999

X-34 Vehicle Aerodynamic Characteristics

Gregory J. Brauckmann*
NASA Langley Research Center, Hampton, Virginia 23681

The X-34, being designed and built by the Orbital Sciences Corporation, is an unmanned suborbital vehicle designed to be used as a flying test bed to demonstrate key vehicle and operational technologies applicable to future reusable launch vehicles. The X-34 will be air-launched from an L-1011 carrier aircraft, where an onboard engine will then accelerate the vehicle to speeds above Mach 7 and altitudes to 250,000 ft. An unpowered entry will follow, including an autonomous landing. A series of wind-tunnel tests on scaled models was conducted in four facilities at the NASA Langley Research Center to determine the aerodynamic characteristics of the X-34. Analysis of these test results revealed that longitudinal trim could be achieved throughout the design trajectory. Longitudinal control effectiveness (elevon, body flap) decreased for Mach numbers greater than one and was nonlinear in the transonic regime. In addition, there was a loss in elevon effectiveness for the largest negative deflection. The rudder effectiveness (of the all-moving vertical tail) decreased for supersonic Mach numbers and with increasing angle of attack, so that at combined high supersonic Mach numbers and high angles of attack the use of reaction control jets may be required. Deployment of the landing gear reduced the elevon effectiveness by 5% and destabilized the vehicle directionally.

Nomenclature

b	= reference span
C_A	= axial-force coefficient
C_D	= drag-force coefficient
C_{D0}	= drag-force coefficient at 0-deg angle of attack
C_L	= lift-force coefficient
$C_{L\alpha}$	= slope of lift coefficient at 0-deg angle of attack
C_l	= rolling-moment coefficient
$C_{l\beta}$	= rolling-moment derivative wrt sideslip angle
C_m	= pitching-moment coefficient
C_{m0}	= pitching-moment coefficient at 0-deg angle of attack
C_N	= normal-force coefficient
C_n	= yawing-moment coefficient
$C_{n\beta}$	= yawing-moment derivative wrt sideslip angle
C_Y	= side-force coefficient
c	= mean aerodynamic chord
M	= Mach number
p	= freestream static pressure, psf
q	= freestream dynamic pressure, psf
Re_c	= length Reynolds number based on mean aerodynamic chord
Re/ft	= freestream unit Reynolds number
S	= reference area
T	= freestream static temperature, °R
Xcg	= longitudinal center of gravity (measured from vehicle nose), in.
α	= angle of attack, deg
β	= angle of sideslip, deg
ΔC_D	= increment in drag-force coefficient
ΔC_m	= increment in pitching-moment coefficient
ΔC_n	= increment in yawing-moment coefficient
$\delta_{\rm bf}$	= body flap deflection, deg
δ_e	= elevon deflection, deg
δ_r	= rudder deflection, deg
$\delta_{\rm sb}$	= speed-brake deflection, deg
σ	= standard deviation

Received July 2, 1998; revision received Dec. 17, 1998; accepted for publication Dec. 20, 1998.

*Research Engineer, Aerothermodynamics Branch, Aero- and Gas-Dynamics Division. Senior Member AIAA.

Introduction

THE X-34 (Ref. 1), being designed and built by the Orbital Sciences Corporation (OSC), is an unmanned suborbital vehicle designed to be used as a flying test bed to demonstrate key vehicle and operational technologies applicable to future reusable launch vehicles (RLVs). The X-34 will be air-launched from an L-1011 carrier aircraft at approximately Mach 0.7 and 38,000-ft altitude. An onboard engine will accelerate the vehicle to speeds above Mach 7 and altitudes to 250,000 ft. An unpowered entry will follow, including an autonomous landing. The X-34 will demonstrate the ability to fly through inclement weather, land horizontally at a designated site, and have rapid turnaround capability. Key technologies used in the construction or operation are composite primary and secondary airframe structures, advanced thermal protection systems (TPS) and materials, a flush air data system, and automated vehicle checkout.

The X-34 vehicle is approximately 54 ft long, with a wingspan of 28 ft. Vehicle dry weight is approximately 18,000 lb. The X-34 planform is similar to the Space Shuttle Orbiter. A double-delta wing with sweep angles of 80 and 45 deg is employed. The wing (as well as the fuselage) has a flat bottom and a constant leading edge radius to facilitate manufacturing. Wing dihedral is 6 deg. The fuselage transitions from a trapezoidal cross section to a rectangular cross section moving downstream from the nose. Control surfaces are the inboard and outboard elevons (on the wing), the body flap (extending off the aft end of the vehicle), and an all-moving vertical tail. The rear portion of the vertical tail incorporates a split-speed brake design, as in the Shuttle.

The present X-34 program started in the summer of 1996. Previously OSC had teamed with Rockwell International on an earlier, larger vehicle, and the current design is based on this work. A short series of wind-tunnel tests (1 subsonic, 1 transonic, and 1 hypersonic) was conducted in the fall of 1996 to assess the current design. These experimental data were used to refine engineering code predictions that formed the initial aerodynamic database. At this time the vehicle aerodynamic characteristics were determined to be acceptable in that controlled flight could be achieved. Because of the fast-paced nature of the program (first flight was to have been in 1998), no further optimization of the aerolines was made, and the vehicle outer mold lines were thus frozen in December 1996. A set of benchmark wind-tunnel tests followed, the results of which are discussed in this paper, to define the final aerodynamic characteristics of the vehicle. The new tests would form the basis for the flight aerodynamic database, replacing the earlier wind-tunnel data and engineering code predictions as each new test was completed. This paper presents the first release of these data and is not intended to be comprehensive but to give an overview of the aerodynamic

characteristics of this configuration. Formal documentation of the complete experimental aerodynamic database is planned.

The nominal trajectory of the X-34 is presented in Fig. 1. The angle of attack, Mach number, Reynolds number, and longitudinal c.g. are shown as functions of time for both the ascent and descent trajectories. On ascent the X-34 maintains a low angle of attack, around 5 deg, except in the initial transonic phase just after drop. Here the vehicle pitches to a higher angle of attack (~13 deg) to rapidly establish a steep flight path angle to pull the vehicle out of the lower atmosphere as quickly as possible. On descent the angle of attack is initially maintained at 25 deg and then is progressively lowered. For this trajectory the maximum Mach number is 7.2 at an altitude of 250,000 ft. The Reynolds number shown in Fig. 1c is based on freestream conditions and the mean aerodynamic chord. Wind-tunnel data were not obtained at flight values of Reynolds numbers except at high supersonic and hypersonic Mach numbers. The longitudinal c.g. (measured from the nose of the vehicle), shown in Fig. 1d, shifts aft, then forward, as fuel is burned. Engine burnout occurs at approximately 145 s. Approximately 480 s into the flight, the residual fuel is dumped, accounting for the slight aft shift in c.g. at this time.

Experimental Method

Models

The majority of the data presented (all except the Mach 0.25 data) were obtained with models representing the latest outer-mold-line (OML) geometry. This geometry was obtained from OSC in Initial Graphics Exchange Specification format and was designated X1001215. Two models were built to these aerolines: a 0.018 scale and a 0.033 scale. A third model, of 0.018 scale, was fabricated prior to this and thus represented the OML of an earlier geometry. The major differences in the aerolines were modifications to the TPS blanket geometry on the later models. Differing thickness of TPS blankets resulted in aft-facing ramps on the upper surface of the wing (approximately 10% back from the leading edge) and also aft-facing ramps in the nose region. The ramp heights were 0.25 in full scale.

All three models were made of aluminum and/or stainless steel, and control-surface deflections were achieved by the use of individual brackets. The all-moving tail deflection was set by use of a locating pin. The speed brakes were attached to the aft section of the tail. For the initial 0.018 model the speed brakes were of a wedge type, whereas for the later models a split-speed brake design was used. Control-surface deflections tested were −30, −20, −10, 0, 10, and 20 deg for the elevons; −15, −10, 0, 10, and 20 deg for the body flap; −5, 0, 10, 20, and 30 deg for the rudder; and 0, 32, 62, and 77 deg for the speed brake. A three-view sketch of the vehicle is given in Fig. 2. Definitions of the control-surface deflections are given in Fig. 3. The reference areas and lengths are given in Table 1.

A partial engine bell was fabricated and tested for each model. The bell was placed at a 15-deg inclination to the waterline, which represented the full upward deflection of the nozzle. This bell had the lower portion removed to prevent fouling with the sting. Landing

Table 1 X-34 reference dimensions

Dimension	Full scale	0.033 scale	0.018 scale
Wing area, ft^2	357.5	0.3972	0.1199
Wing chord, in.	174.5	5.8167	3.1960
Wing span, in.	332.5	11.0833	6.0897
Length, body flap hinge line, in.	649.6	21.6540	11.8978
Inboard elevon area, ft^2	14.5	0.0161	0.0049
Outboard elevon area, ft^2	14.9	0.0166	0.0050
Body flap area, ft^2	22.3	0.0248	0.0075
Vertical tail area, ft^2	33.0	0.0367	0.0111
Speed brake area, ft^2	11.0	0.0122	0.0037

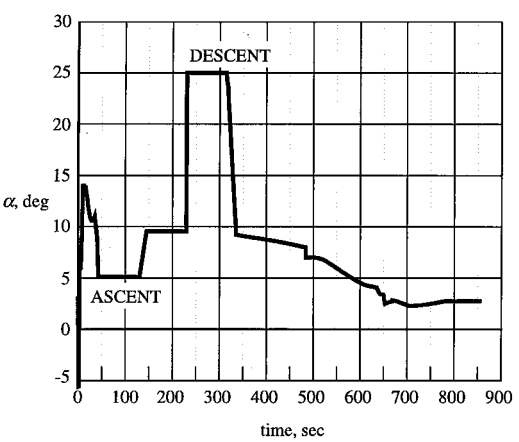

a) Angle of attack

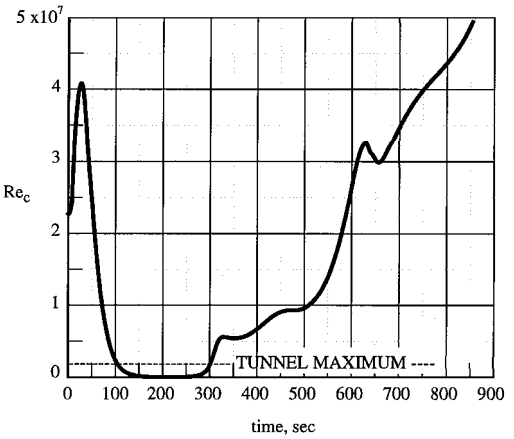

c) Chord Reynolds number

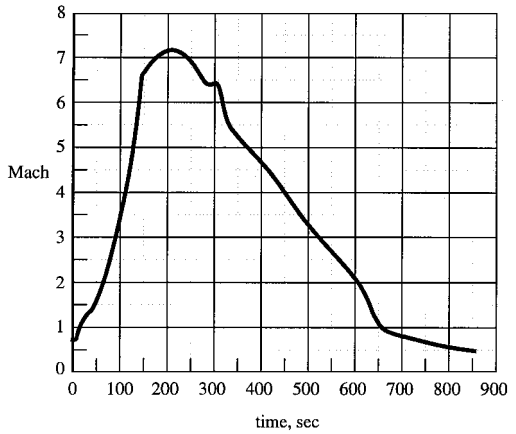

b) Mach number

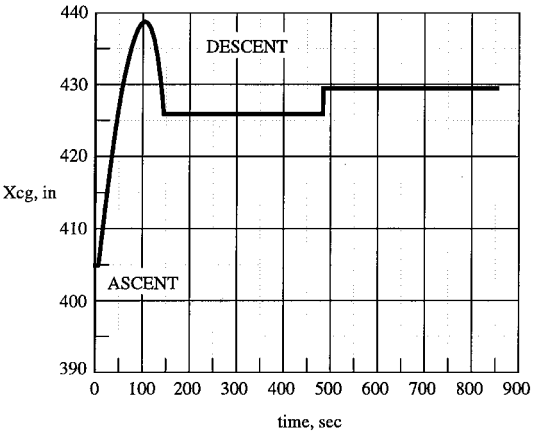

d) Longitudinal c.g.

Fig. 1 X-34 reference trajectory parameters.

Table 2 Nominal flow conditions

Facility	Mach	q, psf	p, psf	T, °R	Re/ft $\times 10^{-6}$	$Re_c \times 10^{-6}$
LTPT	0.25	300	6945	533	5.6	1.5
16-ft TT	0.4	212	1895	567	2.3	1.1
	0.6	418	1659	546	3.1	1.5
	0.8	622	1388	519	3.7	1.8
	0.85	667	1319	511	3.8	1.8
	0.9	709	1251	503	3.9	1.9
	0.925	729	1217	500	4.0	1.9
	0.95	748	1184	496	4.0	1.9
	0.98	769	1144	491	4.0	1.9
	1.05	813	1053	479	4.1	2.0
	1.1	839	991	471	4.1	2.0
	1.25	893	817	446	4.2	2.0
UPWT-1	1.6	910	507	387	4.0	2.0
	1.8	911	402	355	4.0	2.0
	2.0	897	320	325	4.0	2.0
UPWT-2	2.5	870	199	271	4.0	2.0
	3.0	760	121	218	4.0	2.0
	4.0	546	49	145	4.0	2.0
	4.6	436	29	117	4.0	2.0
20-Inch Mach 6	6.0	138	5	108	1.0	0.3
	6.0	287	11	111	2.0	0.5
	6.0	575	23	111	4.0	1.1
	6.0	862	34	114	6.0	1.6

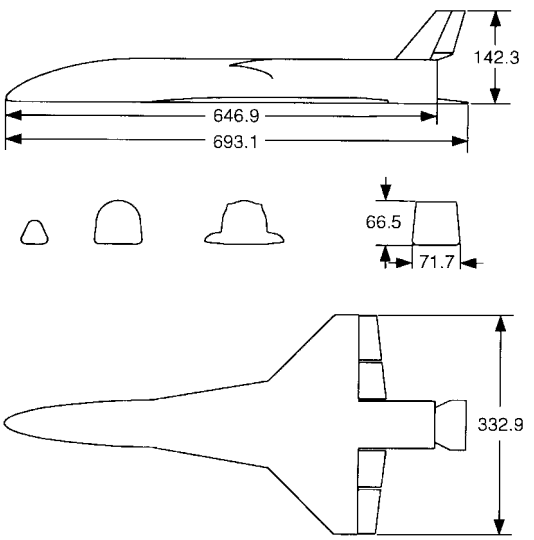

Fig. 2 Sketch of X-34 geometry (dimensions in inches).

gear and doors were fabricated for the initial 0.018 model to examine their effect on aerodynamic performance at Mach 0.25.

Facilities

Four facilities were used to obtain the aerodynamic data presented in this paper. A brief description of each is given. Nominal flow conditions are presented in Table 2.

Langley Research Center Low-Turbulence Pressure Tunnel

The NASA Langley Research Center (LaRC) Low-Turbulence Pressure Tunnel[2] (LTPT) is a single-return, closed-throat pressure tunnel with a 3×7.5 ft test section. Mach number can be varied from 0.15 to 0.3. The tunnel can be pressurized from 1 to 10 atm to vary the unit Reynolds number. Low-turbulence levels are achieved by using a large contraction ratio and a number of fine-wire small-mesh screens in the settling chamber. A pitch/roll mechanism is used to set model attitude. Mach number is determined from measured values of total and static pressures.

LaRC 16-ft Transonic Wind Tunnel

The NASA Langley 16-ft Transonic Tunnel[3] is a closed-circuit, single-return, continuous-flow atmospheric tunnel with a slotted wall test section. The test medium is air with an air exchange for cooling. The normal testing range is Mach numbers from 0.2 to 1.3

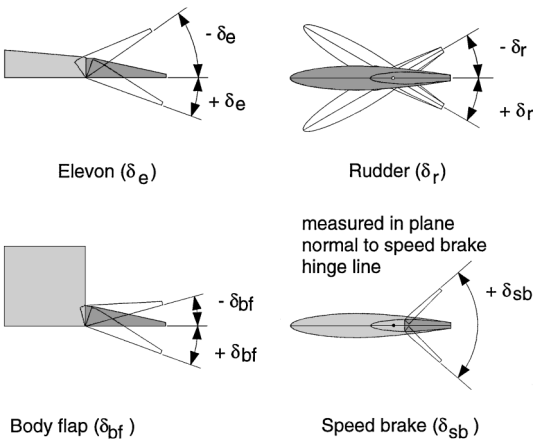

Fig. 3 Definitions of control-surface deflections.

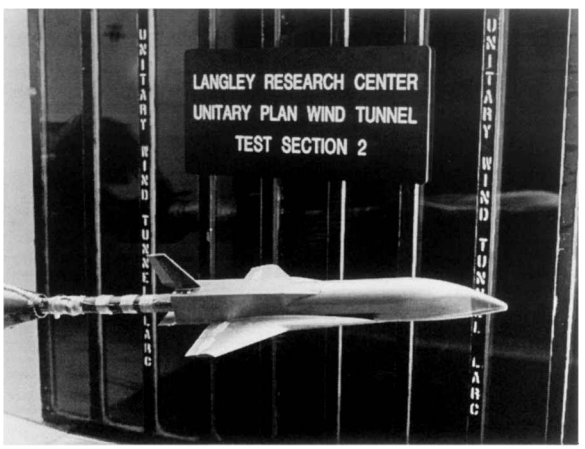

a) Overall view

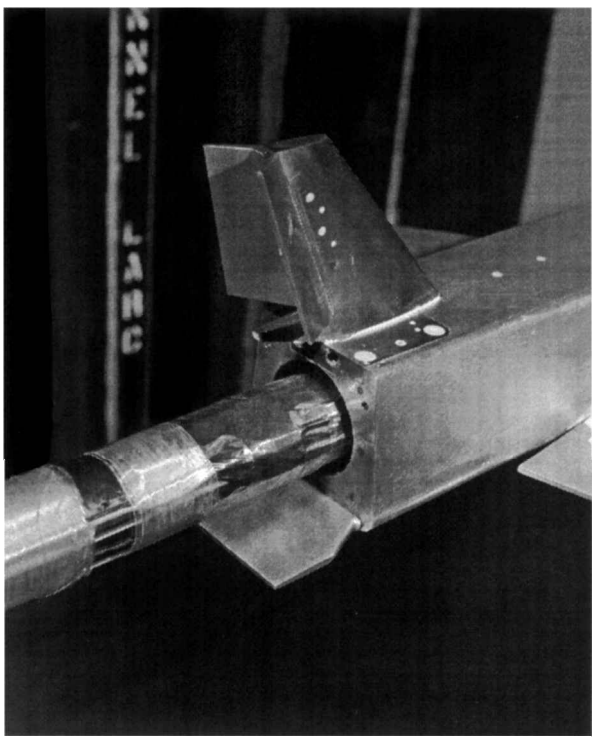

b) Detail of base area and speed brake

Fig. 4 Installation of 0.033-scale X-34 in Unitary Plan Wind Tunnel.

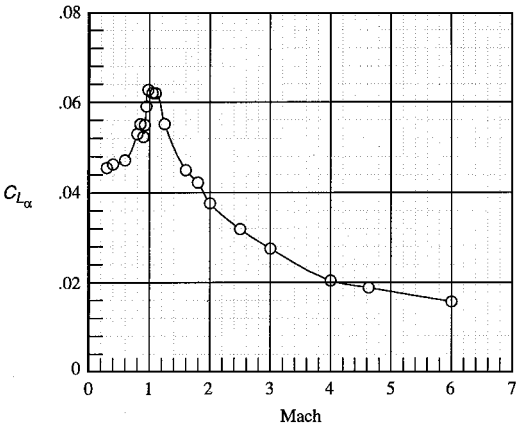

a) $C_{L\alpha}$

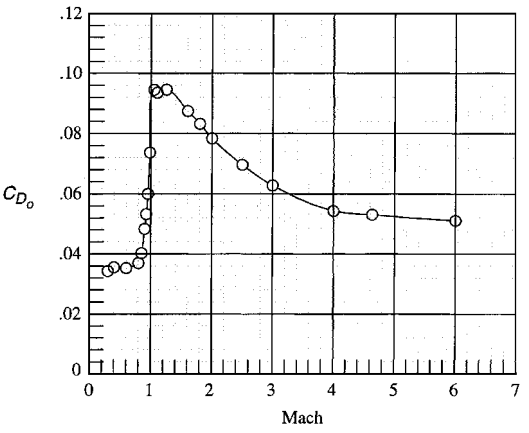

b) C_{D0}

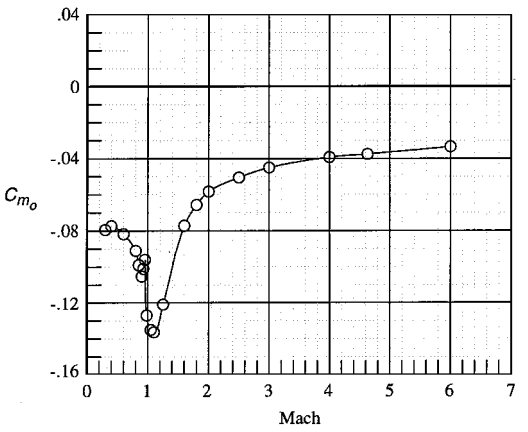

c) C_{m0}

Fig. 5 Baseline longitudinal aerodynamic characteristics.

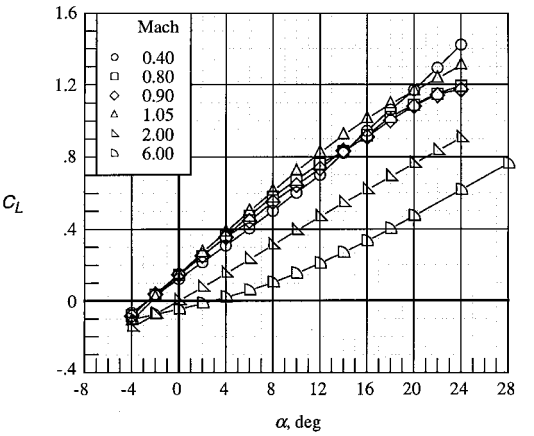

a) C_L

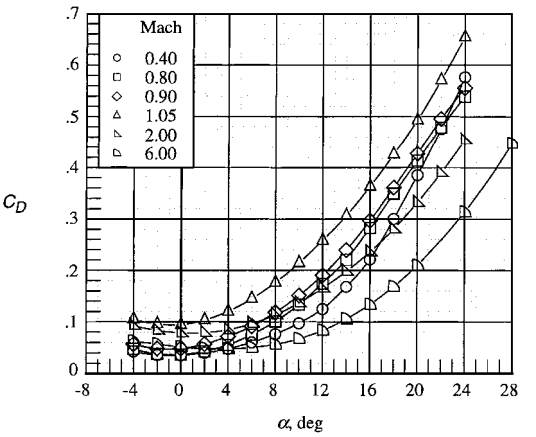

b) C_D

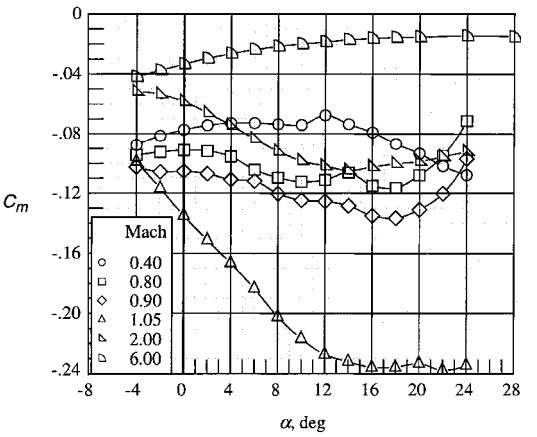

c) C_m

Fig. 6 Baseline longitudinal aerodynamic characteristics.

and angles of attack up to 25 deg. Speeds up to Mach 1.05 are obtained with the tunnel main drive fans; speeds above this are obtained with a combination of main drive fans and test-section plenum suction. The slotted octagonal test section nominally measures 15.5 ft across the flats. The usable test section length is 22 ft for speeds up to Mach 1.0 and 8 ft for speeds above Mach 1.0. Mach number is determined from measured values of total and static pressure.

LaRC Unitary Plan Wind Tunnel

The NASA Langley Unitary Plan Wind Tunnel[4] (UPWT) is a closed-circuit pressure tunnel with two 4×7 ft test sections. The major elements of the facility are the 100,000-hp drive system, a dry air supply and evacuating system, a cooling system, and the interconnecting ducting to provide the proper air flow to either of the two test sections. The tunnel circuit is designed to operate at pressures from near vacuum to 10 atm. The low-Mach-number test section covers the range from 1.46 to 2.86, and the high-Mach-number test section covers the range from 2.3 to 4.63. The nozzle walls are asymmetric, and the lower wall of the nozzle moves longitudinally to provide the necessary variation in area ratio. The model/sting support mechanism is capable of an angle-of-attack range from −12 to 22 deg (with higher angles obtainable with the use of dogleg stings), a sideslip of ±14 deg, and a roll continuous through 310 deg. Mach number is determined from the position of the nozzle block. Calibrations are periodically performed to verify the initial calibration.

LaRC 20-Inch Mach 6 Air Tunnel

The NASA Langley 20-Inch Mach 6 Air Tunnel[5] is a hypersonic blow-down facility that uses heated, dried, and filtered air as the test gas. Typical operating conditions for the tunnel are stagnation pressures from 30 to 500 psia, stagnation temperatures from 750 to 1000°R, and freestream unit Reynolds numbers from 0.5×10^6 to

Table 3 Estimated uncertainties (based on 0.5% balance accuracy)

Facility	Mach	C_N	C_A	C_m	C_l	C_n	C_Y
LTPT	0.25	0.0216	0.0029	0.0092	0.0007	0.0012	0.0072
16-ft TT	0.4	0.0416	0.0051	0.0179	0.0017	0.0040	0.0179
	0.6	0.0211	0.0026	0.0091	0.0009	0.0020	0.0091
	0.8	0.0142	0.0017	0.0061	0.0006	0.0014	0.0061
	0.85	0.0132	0.0016	0.0057	0.0006	0.0013	0.0057
	0.9	0.0125	0.0015	0.0054	0.0005	0.0012	0.0053
	0.925	0.0121	0.0015	0.0052	0.0005	0.0012	0.0052
	0.95	0.0118	0.0014	0.0051	0.0005	0.0011	0.0051
	0.98	0.0115	0.0014	0.0049	0.0005	0.0011	0.0049
	1.05	0.0109	0.0013	0.0047	0.0005	0.0011	0.0047
	1.1	0.0105	0.0013	0.0045	0.0004	0.0010	0.0045
	1.25	0.0099	0.0012	0.0043	0.0004	0.0010	0.0042
UPWT-1	1.6	0.0083	0.0008	0.0043	0.0005	0.0008	0.0028
	1.8	0.0083	0.0008	0.0043	0.0005	0.0008	0.0028
	2.0	0.0084	0.0008	0.0044	0.0005	0.0008	0.0028
UPWT-2	2.5	0.0087	0.0009	0.0045	0.0005	0.0008	0.0029
	3.0	0.0100	0.0010	0.0051	0.0006	0.0009	0.0033
	4.0	0.0139	0.0014	0.0072	0.0008	0.0013	0.0046
	4.6	0.0174	0.0017	0.0090	0.0011	0.0016	0.0058
20-Inch Mach 6	6.0	0.0218	0.0054	0.0069	0.0005	0.0008	0.0045

Table 4 Data repeatability (2σ values)

Facility	Mach	C_N	C_A	C_m	C_l	C_n	C_Y
16-ft TT	0.4	0.0104	0.0028	0.0054	0.0003	0.0003	0.0006
	0.8	0.0118	0.0019	0.0046	0.0008	0.0004	0.0009
	0.9	0.0119	0.0015	0.0058	0.0009	0.0007	0.0010
	0.95	0.0112	0.0015	0.0064	0.0005	0.0008	0.0012
	1.05	0.0078	0.0014	0.0044	0.0004	0.0005	0.0009
	1.25	0.0059	0.0014	0.0035	0.0002	0.0007	0.0010
UPWT-1	1.6	0.0020	0.0001	0.0003	0.0005	0.0008	0.0011
	1.8	0.0018	0.0001	0.0004	0.0003	0.0006	0.0016
	2.0	0.0016	0.0002	0.0003	0.0002	0.0004	0.0009
UPWT-2	2.5	0.0022	0.0008	0.0013	0.0006	0.0008	0.0016
	3.0	0.0021	0.0005	0.0012	0.0005	0.0004	0.0007
	4.0	0.0036	0.0004	0.0014	0.0001	0.0003	0.0008
	4.6	0.0036	0.0004	0.0014	0.0002	0.0004	0.0011
20-Inch Mach 6	6.0	0.0107	0.0012	0.0016	0.0002	0.0002	0.0006

8×10^6/ft. A two-dimensional, contoured nozzle is used to provide nominal freestream Mach numbers from 5.8 to 6.1. The test section is 20.5×20 in.; the nozzle throat is 0.4×20.5 in. A bottom-mounted model injection system can insert models from a sheltered position to the tunnel centerline in less than 0.5 s. Run times up to 15 min are possible with this facility; current test run times were on the order of 2 min. The Mach number was determined from previous facility calibrations, and measured values of pitot pressure were compared to these calibrations to determine whether any significant changes had occurred.

Instrumentation and Test Procedures

Aerodynamic forces and moments were measured with a six-component strain gauge balance. Three different balances were used to manage the load range occurring in the four facilities. All models were sting-mounted through the base. The balance was water-cooled to minimize heating effects in the 20-Inch Mach 6 Tunnel. Data were acquired in a pitch pause manner in all facilities. All tests measured the cavity pressure by use of pressure tubes run along the sting into the model cavity. Base pressures were measured by use of tubes that ran alongside the sting into the base region in the LTPT and 20-Inch Mach 6 Tunnel, and by actual orifices on the base for the other facilities. All axial data are corrected for chamber pressure adjusted to the average base pressure. Corrections for weight tares, balance interactions, and sting deflections are also included. The moment reference center is 420 in. (measured from the nose). Boundary layer transition trips (carborundum grit strips) were used to provide turbulent flow in all facilities except the 20-Inch Mach 6 Tunnel and UPWT test Sec. 2. In these latter two facilities difficulties in tripping the high Mach number flow, as well as the ability to achieve (or nearly so) flight values of Reynolds numbers, led to the decision to not trip the flow artificially. A typical tunnel installation (UPWT-2) is shown in Fig. 4a. Details of the base area including the split speed brake design are shown in Fig. 4b. The initial 0.018-scale model was used in the LTPT facility (Mach 0.25), the 0.033-scale model was tested in the 16-ft Transonic Tunnel and the two legs of the Unitary Plan Wind Tunnel (Mach 0.4–4.63), and the later 0.018-scale model was tested in the 20-Inch Mach 6 Tunnel (Mach 6).

A rigorous uncertainty analysis has not been performed for the wind-tunnel data. An estimate is made by assuming an uncertainty of 0.5% of the balance full-scale loads. The quoted balance accuracies are better (less than 0.25%), but this conservative approach can allow for uncertainties in other parameters such as model attitude and flow uniformity. The estimated uncertainties are presented in Table 3. In addition, data repeatability within each test (series of runs in a given facility) was examined by determining the standard deviation of the error from all repeat points. The two-sigma variations thus determined are presented in Table 4. Data repeatability generally was better or equal to the estimated balance uncertainties except in the transonic regime (some values for C_A and C_m up to 1.3 times the balance uncertainty) and for rolling moment at Mach 0.8, 0.9, and 2.5 (worst case: 1.8 times balance uncertainty at Mach 0.9). The uncertainty estimates do not include any bias error to be included in the final flight database from such sources as protuberance drag, drag due to the blanket roughness, and nonflight Reynolds number.

Results and Discussion

Some of the longitudinal characteristics ($C_{L\alpha}$, C_{D0}, C_{m0}) of the X-34 are shown in Figs. 5a–5c, plotted against Mach number. There

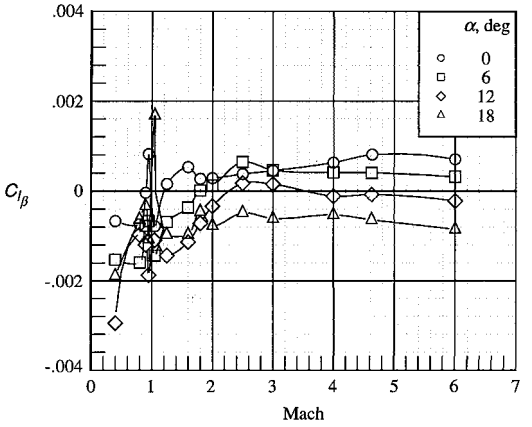

a) $C_{l\beta}$

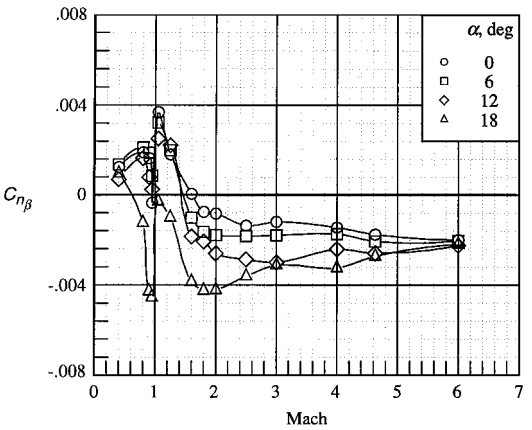

b) $C_{n\beta}$

Fig. 7 Baseline lateral-directional aerodynamic characteristics.

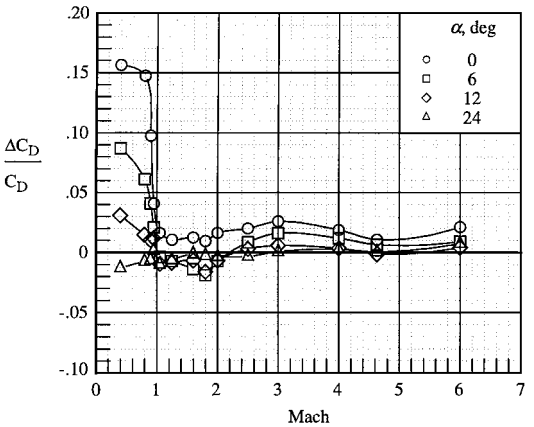

a) $\Delta C_D/C_D$

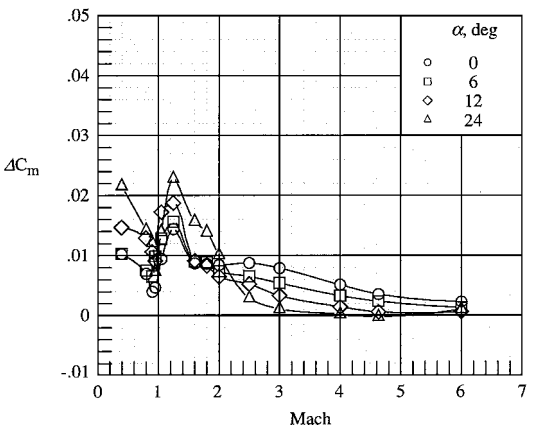

b) ΔC_m

Fig. 8 Effect of engine bell.

is a general increase in $C_{L\alpha}$ with Mach number for the subsonic Mach numbers up to $M = 0.98$, with a noticeable break (decrease) occurring at $M = 0.9$, followed by a steady decrease throughout the supersonic Mach numbers. The initial increase in $C_{L\alpha}$ is attributed to compressibility effects. The break is attributed to shock formation on the vehicle. Flow visualization was not performed to determine the exact cause. C_{D0} experiences the onset of the transonic drag rise above $M = 0.8$. The drag then decreases for Mach numbers above 1.25. Although drag is not of primary importance on descent for vehicles of this type, the acceleration of the vehicle will be affected, limiting the final altitude and Mach number achieved. C_{m0} is negative for all Mach numbers, and this is an indication that negative (up) deflections of the control surfaces will be needed to trim the vehicle longitudinally. The effect of the break in lift (near $M = 0.9$) is seen here as a break in the pitching-moment curve. Lift, drag, and pitching moment are plotted against angle of attack for several Mach numbers in Figs. 6a–6c. The lift curve for $M = 0.4$ is linear up to 12-deg angle of attack, where a change in the slope is seen, due to vortex lift. The hypersonic Mach number lift curve is nonlinear, as is usually the case. A nose-down movement of the pitching-moment curve with increasing Mach number is seen (Fig. 6c), which is very pronounced as the transonic regime is encountered. The pitching moment is then less nose-down as the supersonic and hypersonic Mach numbers are reached.

The lateral-directional stability derivatives $C_{l\beta}$ and $C_{n\beta}$ are shown in Figs. 7a and 7b for several angles of attack. The vehicle is stable in roll (negative values of $C_{l\beta}$) for subsonic Mach numbers (and more so at higher angles of attack, where the wing dihedral is more effective), but is less stable for transonic Mach numbers and above. The vehicle is unstable or neutrally stable for angles of attack less than 12 deg for Mach numbers greater than 1.2. The X-34 is stable directionally (positive values of $C_{n\beta}$) for subsonic Mach numbers and lower angles of attack (typically <16 deg). There is a general decrease in stability as both Mach number and angle of attack increase, primarily due to the tail being shielded by the body. The vehicle is unstable for all angles of attack for Mach numbers greater than 1.6.

The effect of the partial engine bell is presented in Figs. 8a and 8b. For the 15-deg deflection (relative to the waterline) tested, the bell extended above the fuselage upper surface. This deflection of the engine bell will occur only during engine burn when thrust vectoring is used. On descent the engine bell will be at a nominal −5 deg. The effect on drag (presented as a percentage of the total vehicle drag) is only appreciable below Mach 1; otherwise it is less than 3%. The largest effect (16% at $M = 0.4$) occurs at an angle of attack of 0 deg and rapidly decreases to less than 5% for $\alpha > 12$ deg. The bell causes a maximum nose-up increment in pitch of 0.023 at a Mach number of 1.25, which is equivalent to about 2 deg of elevon deflection. At the higher Mach numbers the increment is less than 0.01, but this still represents elevon deflections of up to 4 deg (at $M = 3$) because the elevon effectiveness is less at the higher Mach numbers.

The elevon effectiveness is shown in Figs. 9a–9d for several angles of attack. The increments in C_m shown are those between a deflected configuration and the baseline ($\delta_e = 0$ deg). In general the elevon effectiveness increases with Mach number up to $M = 1$, then decreases for supersonic Mach numbers. The data are presented again in Figs. 9e–9h for a smaller range of Mach numbers to highlight the changes that occur in the transonic regime. Several trends are noted. There is a definite loss of effectiveness for the −30-deg deflection. In fact, for the two highest angles of attack shown ($\alpha = 12$ and 24 deg) the effectiveness is the same as for the −20-deg deflection. This loss is probably due to leeside separation of the wing caused by the rather large flap deflection. In addition, the effectiveness for all deflections is highly nonlinear as the Mach number approaches unity.

The body flap effectiveness is shown in Figs. 10a–10d for several angles of attack. The increments in C_m shown are those between a deflected configuration and the baseline ($\delta_e = 0$ deg). The body flap is less effective than the elevons as a longitudinal control surface, but the trends with Mach number are the same.

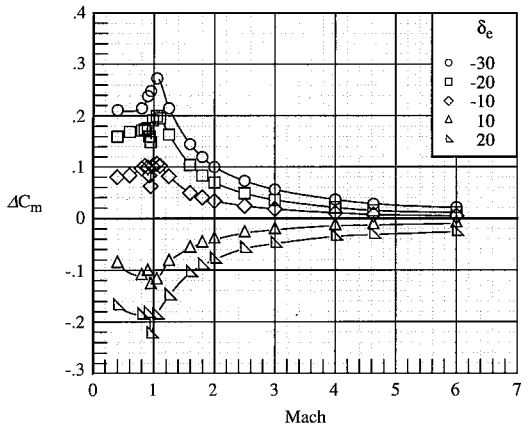

a) $\alpha = 0$ deg

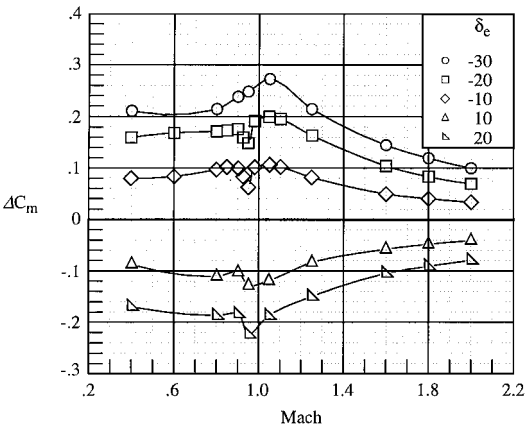

e) $\alpha = 0$ deg

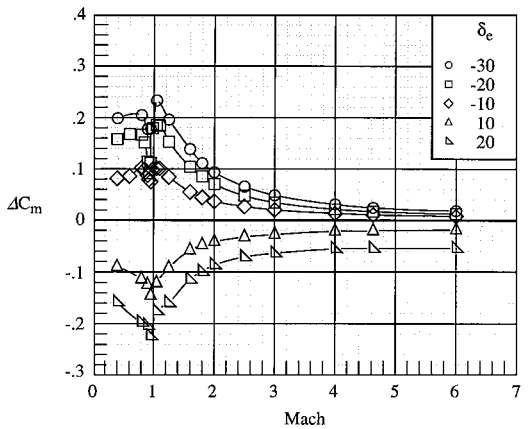

b) $\alpha = 6$ deg

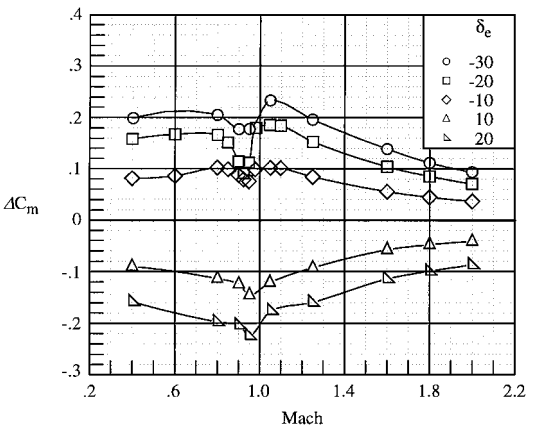

f) $\alpha = 6$ deg

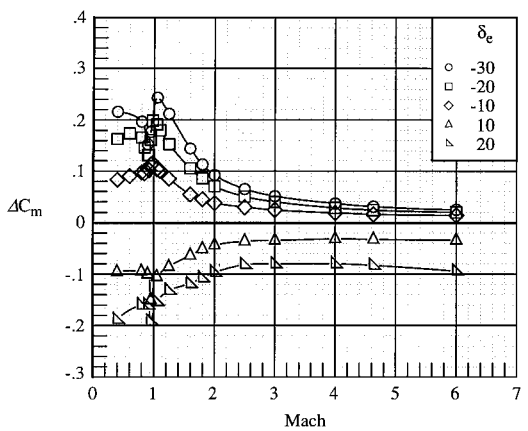

c) $\alpha = 12$ deg

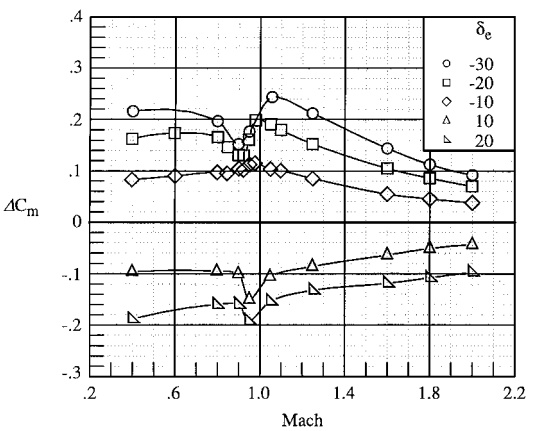

g) $\alpha = 12$ deg

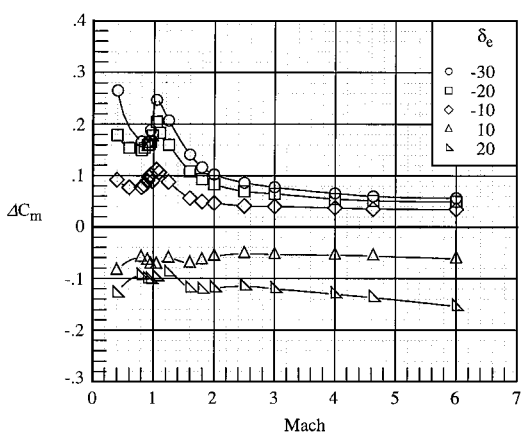

d) $\alpha = 24$ deg

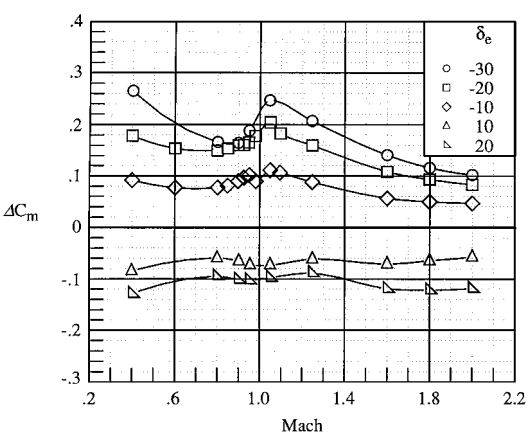

h) $\alpha = 24$ deg

Fig. 9 Effect of elevon deflection.

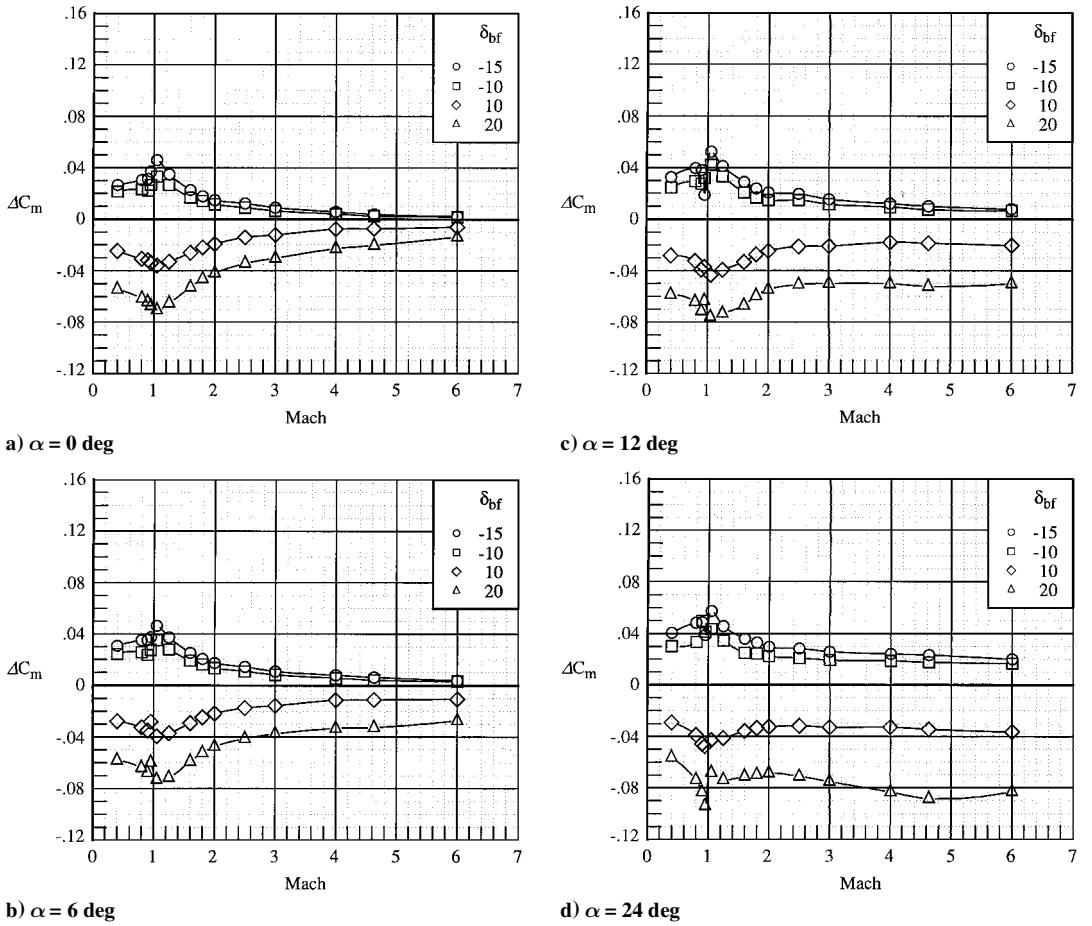

a) $\alpha = 0$ deg

c) $\alpha = 12$ deg

b) $\alpha = 6$ deg

d) $\alpha = 24$ deg

Fig. 10 Effect of body-flap deflection.

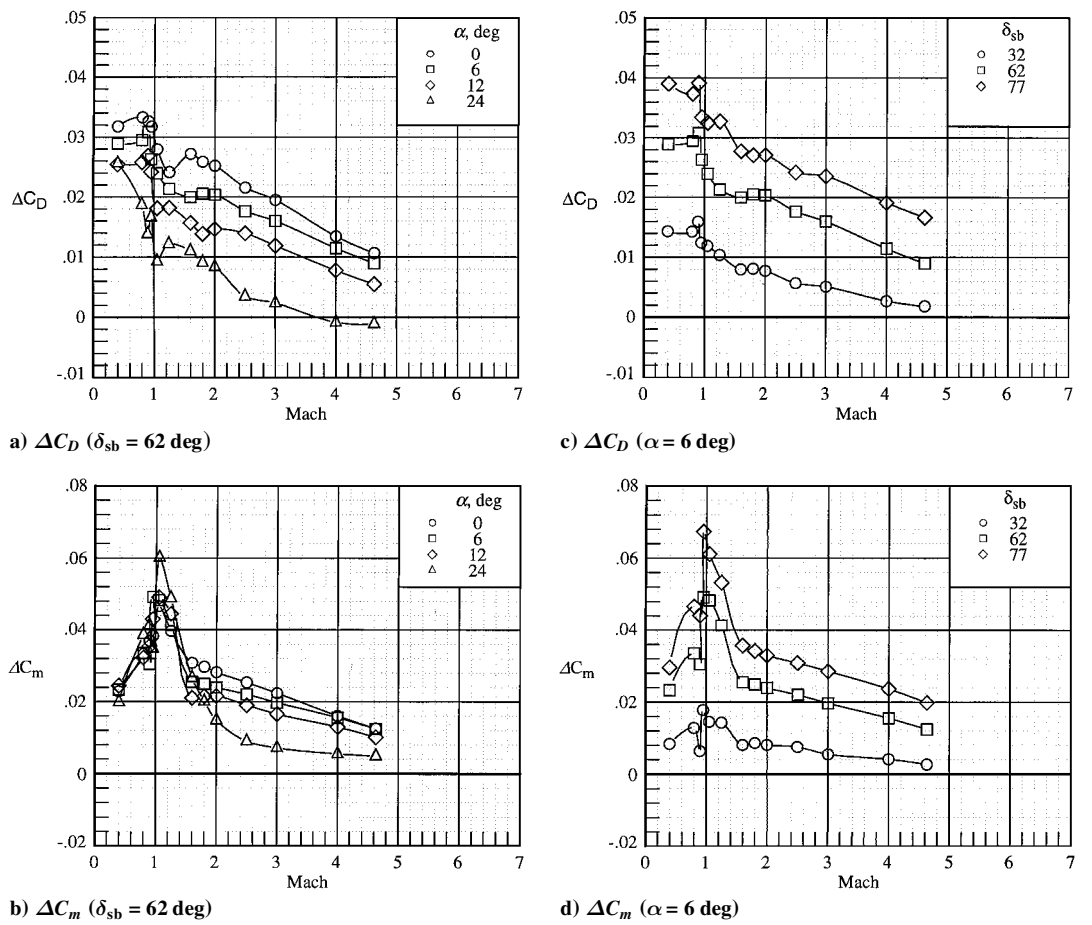

a) ΔC_D ($\delta_{sb} = 62$ deg)

c) ΔC_D ($\alpha = 6$ deg)

b) ΔC_m ($\delta_{sb} = 62$ deg)

d) ΔC_m ($\alpha = 6$ deg)

Fig. 11 Effect of speed-brake deflection.

The speed brakes are intended as an energy management device but also will play an important role in providing longitudinal trim. The speed brakes are not intended to be used above $M = 3$ because of heating concerns, although they were tested up to $M = 4.6$. The increments in C_D and C_m with Mach number are shown in Figs. 11a and 11b for several angles of attack for a single-speed brake deflection of 62 deg. There is a general decrease in drag with Mach number and with angle of attack. The pitching-moment increment is shown in Fig. 11b. There is no monotonic trend with Mach number, with the maximum increment occurring at $M = 1.05$; this implies that the speed brake is also affecting the flow on the fuselage upper surface, and possibly the wing or other areas. The effect of deflection angle for a single angle of attack ($\alpha = 6$ deg) is shown in Figs. 11c and 11d. The data are well behaved and progress in a nearly linear fashion, except around $M = 1$.

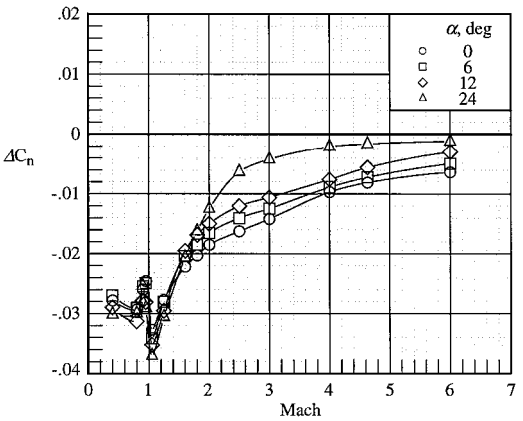

Fig. 12 Effect of rudder deflection (δ_r = 10 deg).

The rudder effectiveness (ΔC_n) is shown in Fig. 12 for a 10-deg rudder deflection. Rudder effectiveness for the subsonic and transonic Mach numbers is generally constant with angle of attack. At supersonic Mach numbers, and more so for hypersonic Mach numbers, the rudder effectiveness decreases with angle of attack and is ineffective above 20-deg angle of attack for the highest Mach number. This result will necessitate the use of reaction control jets for portions of the trajectory. The rudder is more effective as the Mach number increases up to $M = 1.05$, then the effectiveness decreases with the Mach number.

The effectiveness of the rudder and that of the speed brakes are mutually affected. Figures 13a–13d present the increment in C_n for the rudder deflected -5 deg with and without a 62-deg speed brake deployed. Rudder effectiveness is degraded for subsonic Mach numbers but is actually more effective with the speed brake deployed for supersonic Mach numbers. This trend holds true throughout the angle-of-attack range. This trend can be understood by assuming that subsonically the deflected brake separates the flow on the tail, causing it to generate less lift. Supersonically, the increased pressure due to the wedge shock increases the tail effectiveness.

The overall angle-of-attack trim capability of the X-34 is presented in Figs. 14a–14d. The angle-of-attack range was limited to that tested; namely, -4 to 24 deg (32 deg above Mach 2.5). The results for full control authority ($\delta_e = -30/+20$ deg, $\delta_{bf} = -15/+20$ deg, $\delta_{sb} = 77$ deg) are presented in Figs. 14a and 14b, and those for $\frac{2}{3}$ control authority ($\delta_e = -20/+13$ deg, $\delta_{bf} = -10/+13$ deg, $\delta_{sb} = 62$ deg) are presented in Figs. 14c and 14d. Using less than the maximum control deflection leaves a margin for aerodynamic uncertainties, gust alleviation, etc. For the aft c.g. location (Figs. 14a and 14c) the X-34 can trim at any angle of attack at any Mach number, with the exception of low angles of attack ($\alpha \leq 6$ deg) for Mach numbers greater than 2. The use of the speed brake enlarges this domain slightly. For the forward c.g. location and full control authority (Fig. 14b) the angle of attack is limited

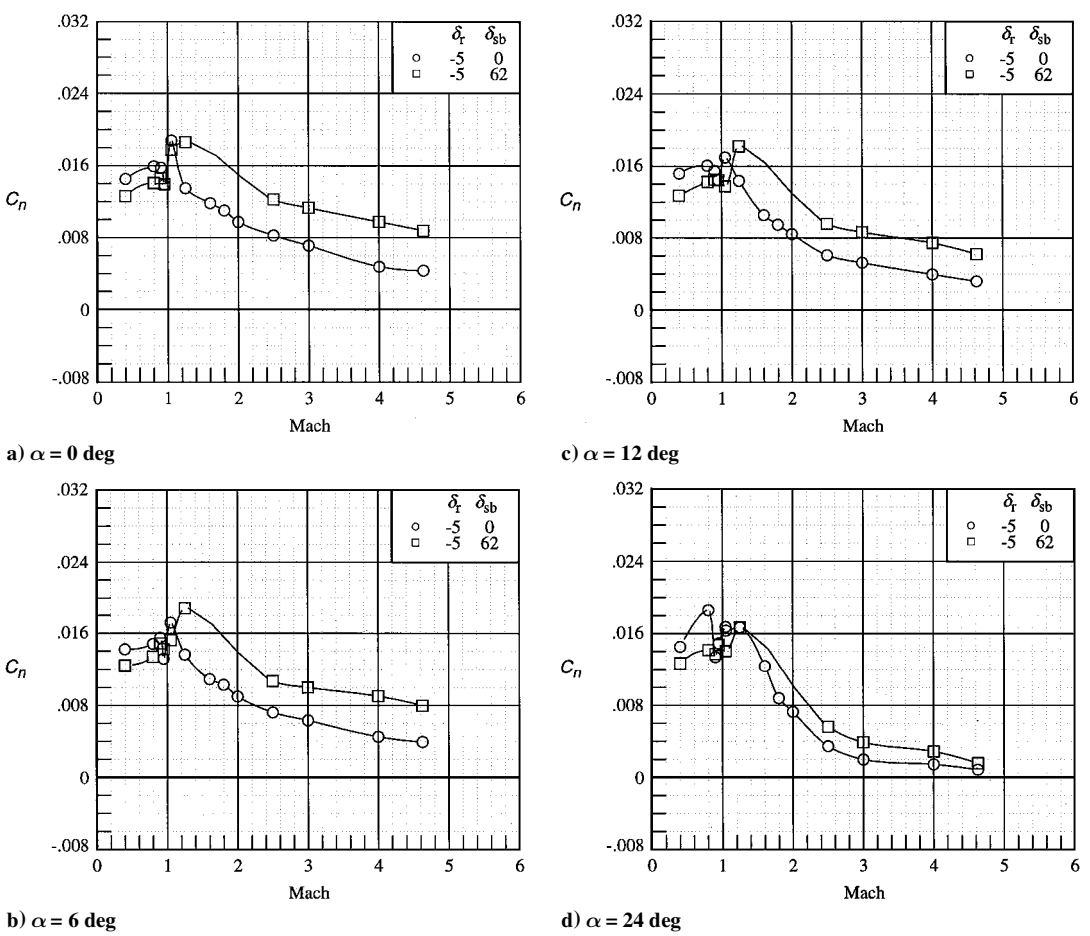

a) α = 0 deg **c) α = 12 deg**

b) α = 6 deg **d) α = 24 deg**

Fig. 13 Effect of combined rudder/speed-brake deflection.

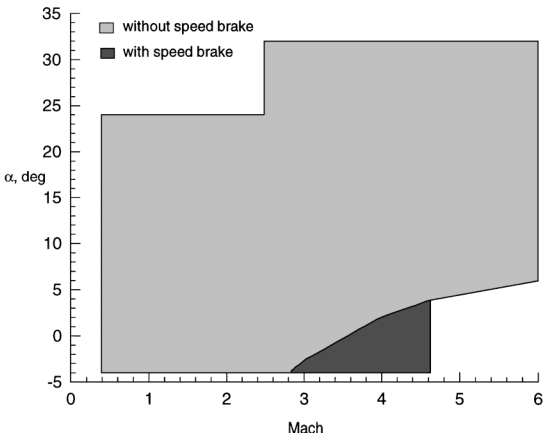

a) Aft c.g., full control authority

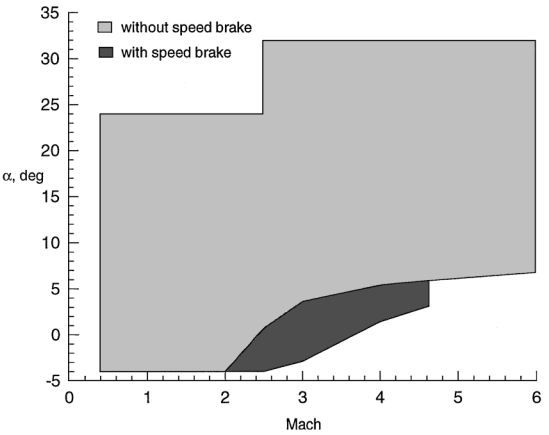

c) Aft c.g., $\frac{2}{3}$ control authority

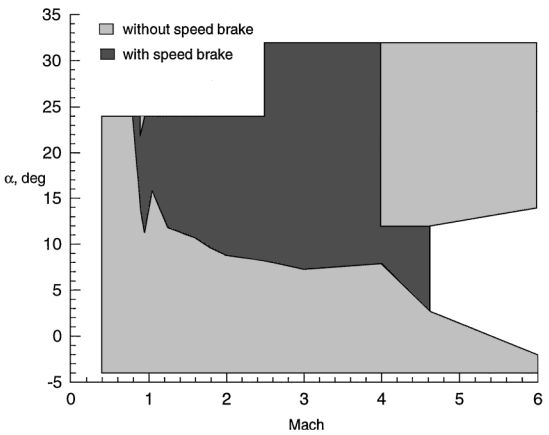

b) Forward c.g., full control authority

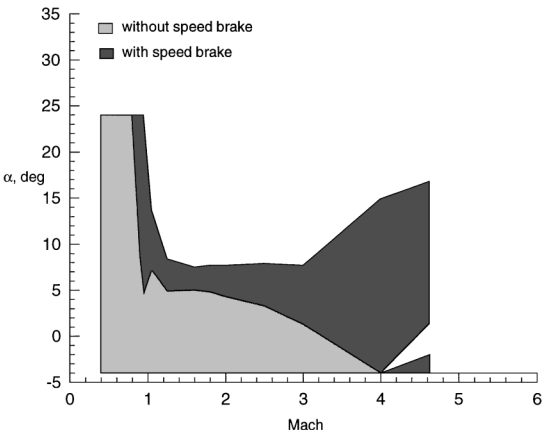

d) Forward c.g., $\frac{2}{3}$ control authority

Fig. 14 Longitudinal trim capability.

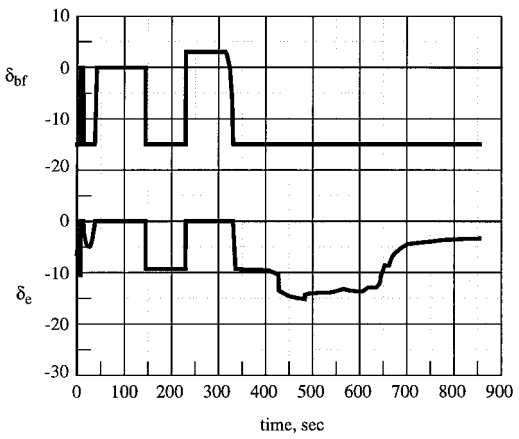

a) Without use of speed brake

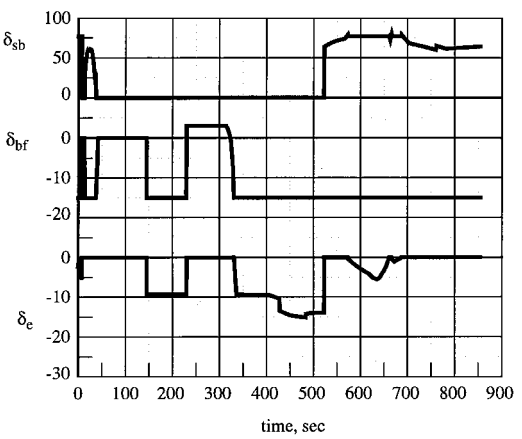

b) With use of speed brake

Fig. 15 Time history of control-surface deflections.

above $M = 0.9$, decreasing from $\alpha = 24$ deg at $M = 0.9$, to approximately 13 deg at $M = 1$, to 8 deg at $M = 4$, and to -2 deg at $M = 6$. Above $M = 4$ the vehicle also can trim at high angles of attack, from $\alpha = 12$–32 deg. Use of the speed brake removes any restrictions on angle of attack. With $\frac{2}{3}$ control authority the restrictions are more severe, with angle of attack limited to 5 deg for Mach numbers greater than 1. The speed brake improves the situation but does not completely eliminate the restrictions.

The time histories of the control-surface deflections for the reference trajectory (Fig. 1) are presented in Figs. 15a and 15b for flight without and with use of the speed brake, respectively. Note that these data are adjusted to the flight c.g. A computer program that simply calculates the deflections needed to achieve trim was used and was not a true flight simulation. A hierarchical use of control surfaces was assumed as follows: thrust vectoring, body flap deflection, speed brake deflection, and finally elevon deflection. As seen, the control surfaces are always deflected in the negative, or up direction. The body flap is deflected to its maximum up position (-15 deg) for most of the trajectory, and the maximum elevon deflection is -15 deg. This deflection is only half the maximum elevon deflection available, leaving a margin for gust alleviation and aerodynamic coefficient uncertainty. The use of the speed brake does not affect the maximum elevon or body flap deflections required, just their duration, because the speed brake is only used below Mach 3.

The effect of landing gear was briefly examined at $M = 0.25$ in the LTPT. The effect of the gear on the lateral-directional characteristics of the X-34 is seen in Fig. 16. Cn_β is seen to change from positive stability (for $\alpha < 14$ deg) to negative stability when the gear

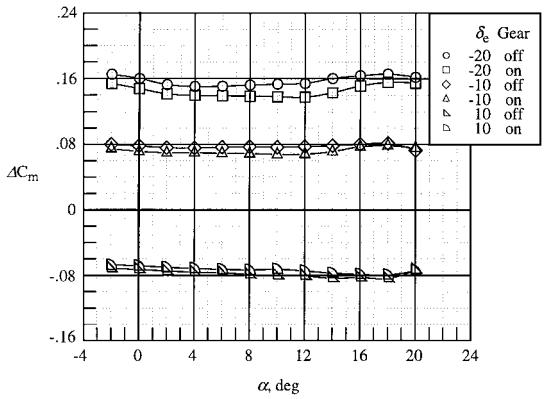

Fig. 16 Effect of landing gear on elevon effectiveness.

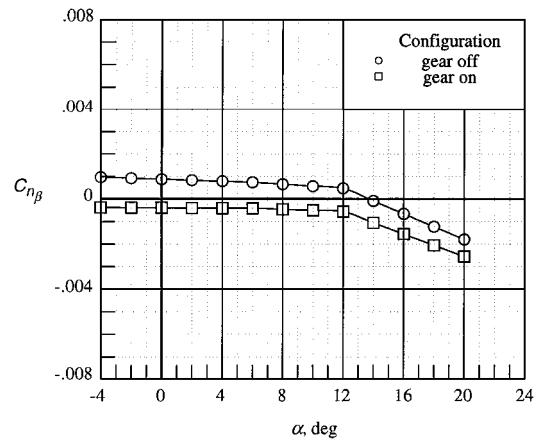

Fig. 17 Effect of landing gear on low-speed directional stability.

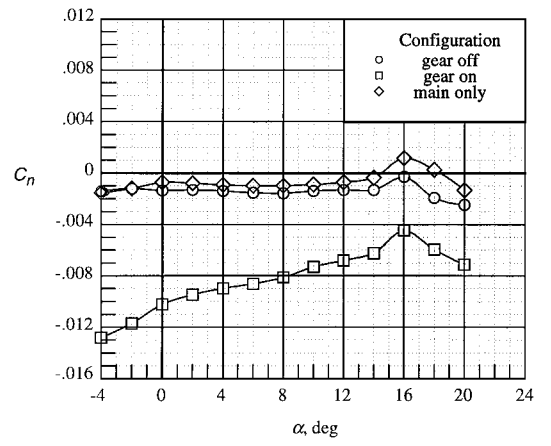

Fig. 18 Effect of nose gear on low-speed directional stability.

is deployed, which can be attributed to the nose gear and its forward location relative to the c.g. In addition, the nose gear causes a yawing moment even at 0-deg sideslip, as seen in Fig. 17. This moment is not present when only the main gear is deployed. The nose gear pressurizes the nose gear door, of which there is only one, situated to the left of the vehicle centerline.

The effect of landing gear on elevon effectiveness is seen in Fig. 18. The elevon effectiveness is reduced by an average of 9% (maximum reduction is 13.8%) for the negative deflections ($\delta_e = -20, -10$ deg), which corresponds to approximately 1–2 deg of elevon deflection to compensate. The reduction is about 6% for the positive deflection (maximum reduction of 10.2%).

Conclusions

A series of wind-tunnel tests on scaled models was conducted in four facilities at the NASA Langley Research Center to determine the aerodynamic characteristics of the X-34. Analysis of these test results revealed that longitudinal trim could be achieved throughout the design trajectory. The maximum elevon deflection required to trim was only half of that available, leaving a margin for gust alleviation and aerodynamic coefficient uncertainty.

Longitudinal control effectiveness (elevon, body flap) decreased for Mach numbers greater than 1 and was nonlinear in the transonic regime. In addition, there was a loss in elevon effectiveness for the largest negative deflection. The rudder effectiveness also decreased for supersonic Mach numbers and with increasing angle of attack. At combined high supersonic Mach numbers and high angles of attack the rudder effectiveness is so small that use of reaction control jets may be required. The rudder and speed brake interacted aerodynamically, decreasing rudder effectiveness for subsonic Mach numbers, but increasing it for supersonic Mach numbers.

Deployment of the landing gear reduced the elevon effectiveness by 9% and also destabilized the vehicle directionally. In addition, the landing gear caused a yawing moment at 0-deg sideslip angle, presumably due to pressurization of the single-nose gear door.

Acknowledgment

I would like to thank Henri Fuhrmann of Orbital Sciences Corporation for his assistance in providing information for this paper.

References

[1]Lindberg, R. E., and Feconda, R. T., "X-34: A Test Bed for RLV Technology," *Aerospace America*, Aug. 1998, pp. 30–33.

[2]McGhee, R. J., Beasley, W. D., and Foster, J. M., "Recent Modifications and Calibration of the Langley Low-Turbulence Pressure Tunnel," NASA TP-2328, July 1984.

[3]Capone, F. J., Bangert, L. S., Asbury, S. C., Mills, C. T., and Bare, E. A., "The NASA Langley 16-Foot Transonic Tunnel," NASA TP-3521, Sept. 1995.

[4]Jackson, C. M., Corlett, W. A., and Monta, W. J., "Description and Calibration of the Langley Unitary Plan Wind Tunnel," NASA TP-1905, Nov. 1981.

[5]Micol, J. M., "Hypersonic Aerodynamic/Aero-Thermodynamic Testing Capabilities at Langley Research Center: Aerothermodynamic Facilities Complex," AIAA Paper 95-2107, June 1995.

T. C. Lin
Associate Editor